CrossMark

# Nonisothermal decomposition kinetics of pure and Mn-doped $Fe_3O_4$ nanoparticles

Tasmira J. Malek[1] · S. H. Chaki[1] · J. P. Tailor[2] · M. P. Deshpande[1]

## Abstract

Pure $Fe_3O_4$ and Mn-doped $Fe_3O_4$ nanoparticles were synthesized by simple wet chemical reduction technique using nontoxic precursors. Manganese doping of two concentrations, 10 and 15%, were employed. All the three synthesized nanoparticles were characterized by stoichiometry, crystal structure, and surface morphology. Thermal studies on as-synthesized nanoparticles of pure ferrite ($Fe_3O_4$) and manganese (Mn) doped ferrites were carried out. The thermal analysis of the three as-synthesized nanoparticles was done by thermogravimetric (TG), differential thermogravimetric, and differential thermal analysis techniques. All the thermal analyses were done in nitrogen atmosphere in the temperature range of 308–1233 K. All the thermocurves were recorded for three heating rates of 10, 15, and 20 K min$^{-1}$. The TG curves showed three steps thermal decomposition for $Fe_3O_4$ and two steps thermal decompositions for Mn-doped $Fe_3O_4$ nanoparticles. The kinetic parameters of the three as-synthesized nanoparticles were evaluated from the thermocurves employing Kissinger–Akahira–Sunose (KAS) method. The thermocurves and evaluated kinetic parameters are discussed in this paper.

**Keywords** Ferrite · Thermogravimetric · Differential thermogravimetric · Differential thermal analysis · Kinetic parameters

## Introduction

Ferrite ($Fe_3O_4$) has an inverse spinel structure and shows ferrimagnetic properties. The octahedral sites of the structure are occupied by $Fe^{2+}$ and $Fe^{3+}$ ions, whereas the tetrahedral sites are occupied by $Fe^{3+}$ ions only [1]. The number of $Fe^{3+}$ ions at the tetrahedral and octahedral sites is equal and possesses opposite spins. Thus, they cancel each other leaving the octahedral site $Fe^{2+}$ ion spins to contribute to the resultant magnetic moment. The ferrite nanoparticles have potential technological applications ranging as of in magnetically guided drug delivery, in magnetic resonance imaging (MRI), as magnetic recording media, as magnetic fluids for the storage and/or retrieval of information, as catalyst, as sensors, as pigments, etc. [2].

Study shows that the particle size and the magnetic properties of the ferrites regulate the application. The other limitation in case of ferrites is that the magnetic iron oxide ($Fe_3O_4$ and $\gamma$-$Fe_2O_3$) nanoparticles undergo phase transition to nonmagnetic phase ($\alpha$-$Fe_2O_3$) when taken to temperature above 750 K. Thus, the phase transition at about 750 K hinders the use of the magnetic properties of the material at high temperature [3]. In the transition from magnetite ($Fe_3O_4$) to maghemite ($\gamma$-$Fe_2O_3$), the crystal structure remains inverse spinel, but for charge compensation, the vacant cation sites appear at the octahedral positions [4]. Further transition from maghemite ($\gamma$-$Fe_2O_3$) to hematite ($\alpha$-$Fe_2O_3$), the structure changes to rhombo-hedrally centered hexagonal configuration of the corundum type in which two-thirds of the octahedral sites are occupied by $Fe^{3+}$ ions. The neighboring spins belonging to different magnetic sublattices are aligned in an almost antiparallel manner and canted by about 5°, leaving a weak ferromagnetic moment pointing in a direction perpendicular to the basal plane. Thus, $\alpha$-$Fe_2O_3$ is said to behave as a weak ferromagnet or a canted antiferromagnet [4]. Therefore, for applications beyond phase transition temperatures

✉ Tasmira J. Malek
  tasmirasybsc02@yahoo.co.in

1  P. G. Department of Physics, Sardar Patel University, Vallabh Vidyanagar, Gujarat 388120, India

2  Applied Physics Department, S.V.N.I.T., Surat, Gujarat 395007, India

(> 750 K), the augmentation of $\gamma$-$Fe_2O_3$ (maghemite) to $\alpha$-$Fe_2O_3$ (hematite) phase transition temperature is a prerequisite. The transition temperature is dependent on several physicochemical parameters [4]. Studies showed that a protective layer of magnetite nanoparticles enhances the $\gamma$-$Fe_2O_3$ to $\alpha$-$Fe_2O_3$ phase transition temperatures [5, 6]. Investigation showed that doping too enhances the phase transition temperature [7–12]. Different elements like Co, Ni, Zn, Cu, Mn, Cr, and Al have been used as dopants [13]. The $\gamma$-$Fe_2O_3$ to $\alpha$-$Fe_2O_3$ phase transition temperature was found to increase to 913 K by 1% Zn doping [14]. It has been observed that the transition temperature has increased to $\sim$ 839, 843, 871, and 874 K by doping with 0.09% of Cu, 0.37% of Co, 0.48% of Ni, and 0.89% of Mn, respectively [15]. Lai et al. [16] studied the effect of Mn(III) doping on $\gamma$-$Fe_2O_3$ to $\alpha$-$Fe_2O_3$ phase transition at ambient atmosphere. Recently, it was observed that $\gamma$-$Fe_2O_3$ nanoparticles dispersed in silica matrix have a high resistance against grain growth and transforms into hematite at 1113 K [17]. Thus, ferrite has been doped by different elements to tailor the phase transition temperature.

Varied numbers of techniques have been used to synthesize $Fe_3O_4$ and doped $Fe_3O_4$ nanoparticles [18–21]. They include sol–gel method [18], co-precipitation [19], reverse micelles [20], and hydrothermal [21]. The authors synthesized pure $Fe_3O_4$ and Mn-doped $Fe_3O_4$ nanoparticles by simple cost-effective routes using cheap and nontoxic precursors [22, 23]. Detailed thermal decomposition kinetics of the synthesized $Fe_3O_4$ and Mn-doped $Fe_3O_4$ nanoparticles which is of great importance for the study of the thermal stability of $Fe_3O_4$ and Mn-doped $Fe_3O_4$ has been carried out in this paper.

The thermal studies on the as-synthesized pure and Mn-doped $Fe_3O_4$ nanoparticles were carried out by measuring the thermocurves. The kinetic study of the nonisothermal outcome for decomposition procedure of the synthesized $Fe_3O_4$ and Mn-doped $Fe_3O_4$ nanoparticles was carried out by applying the isoconversional Kissinger–Akahira–Sunose (KAS) method [24–26]. Such study on pure $Fe_3O_4$ nanoparticles and Mn-doped $Fe_3O_4$ nanoparticles is reported for the first time.

# Experimental

## Synthesis

The pure $Fe_3O_4$ and two Mn (10 and 15%) doped $Fe_3O_4$ nanoparticles were synthesized by simple wet chemical reduction technique. The pure $Fe_3O_4$ nanoparticles synthesis was carried out by taking 10 mL of 2.5 mol sodium borohydride ($NaBH_4$; Sisco Chem, Mumbai, India) solution in a 100-mL glass beaker. It was added dropwise to 40 mL of 0.1 mol ferric chloride hexahydrate ($FeCl_3 \cdot 6H_2O$; Loba Chemie, Mumbai, India) solution under constant stirring. On gradual addition of ferric chloride solution, the final solution slowly turned darker and ultimately became complete black. This happened within less than 1 min after the addition of complete ferric chloride solution. The reaction was considered complete once the bubble generation ceased. The final solution was filtered to obtain pure $Fe_3O_4$ nanoparticles. The obtained nanoparticles were given multiple washes with double-distilled water and absolute methanol. The obtained pure $Fe_3O_4$ nanoparticles were dried overnight at 50 °C in oven [22].

In the two Mn (10 and 15%) doped $Fe_3O_4$ nanoparticles synthesis, firstly 10 mL of 2.5 mol sodium borohydride ($NaBH_4$) solution was taken in a 100-mL glass beaker. Slowly dropwise 40 mL of 0.12 mol ferric chloride hexahydrate ($FeCl_3 \cdot 6H_2O$) solution was added under constant stirring. Both the chemicals used were of make as mentioned in case of pure $Fe_3O_4$ nanoparticles synthesis. After 10 min of vigorous stirring of above solution and under stirring only, 10 mL of 0.18 mol and 0.20 mol manganese chloride tetrahydrate ($MnCl_2 \cdot 4H_2O$; Chiti-chem, Vadodara, India) solution was added to it to get 10 and 15% Mn-doped $Fe_3O_4$ nanoparticles, respectively. The optimization of chemical proportions for synthesis was achieved by means of trial and error. Nine and six trials were carried out to optimize the 10 and 15% Mn-doped $Fe_3O_4$ nanoparticles, respectively. With the addition of all three solutions, the final solutions became darker and eventually turned into complete black within 1 min. The reaction was considered to be complete once the bubble formation stopped. The above reaction leads to the production of Mn (10 and 15%) doped $Fe_3O_4$ nanoparticles, borohydroxide, sodium chloride, and hydrogen gas. The generated hydrogen gas was responsible for the formation of bubbles. The synthesized Mn (10 and 15%) doped $Fe_3O_4$ nanoparticles were given multiple washes with double-distilled water and methanol. The nanoparticles yields were dried overnight in oven at 50 °C [23].

## Characterization

The X-ray energy dispersive analysis (EDAX) technique attached to Philips XL-30 ESEM scanning electron microscope was employed for stoichiometric elemental determination of the synthesized nanoparticles. The crystal structure of the nanoparticles was ascertained by powder X-ray diffraction (XRD) technique. The XRD of the nanoparticles was done using Philips X'Pert MPD X-ray diffractometer employing graphite monochromatized CuK$_\alpha$ radiation ($\lambda$ = 1.5405 Å). The XRD patterns were recorded in the $2\theta$ range of 10° to 90° with scanning rate of 10° min$^{-1}$. The surface morphology study was carried out

using scanning electron microscopy (SEM) employing SEM LEO 1430 VP attached with in-lens SE detector for high-resolution topographic imaging.

The thermal studies on the as-synthesized pure $Fe_3O_4$ nanoparticles and Mn-doped $Fe_3O_4$ nanoparticles were carried out. The thermogravimetry (TG), differential thermogravimetry (DTG), and differential thermal analysis (DTA) curves of the as-synthesized nanoparticles were recorded simultaneously. The thermocurves were recorded in the temperature range from 308 to 1233 K. Three heating rates of 10, 15, and 20 K min$^{-1}$ were employed for the measurement of thermocurves. All thermocurves were measured in nitrogen atmosphere using Seiko SII-EXSTAR TG/DTA-7200 thermal analyzer with gas flow rate of 100 mL min$^{-1}$. The sample mass was kept between 10 and 11 mg for all the three samples.

## Results and discussion

### EDAX

The elemental composition was determined by the energy dispersive analysis of X-ray (EDAX) technique of the as-synthesized pure $Fe_3O_4$ and 10 and 15% Mn-doped $Fe_3O_4$ nanoparticles. The EDAX was done for five different spots on each of the samples, and the average of the five spots was taken as EDAX data of that sample. The obtained elemental EDAX data along with the standard data are given in Table 1 . The data show that the nanoparticles samples are in perfect stoichiometry.

### XRD analysis

The structural characterization of the as-synthesized nanoparticles samples was done by X-ray diffraction (XRD) technique. The recorded XRD patterns are shown in Fig. 1a. The XRD analysis using Powder-X software showed that the samples possess cubic structure with lattice parameters, Table 2, in good agreement with the reported data (JCPDS: 01-88-0315). The analysis of the obtained

lattice parameter shows that the value is highest for pure $Fe_3O_4$ and decreases for 10% Mn-doped $Fe_3O_4$ followed by an increase in the value for 15% Mn-doped $Fe_3O_4$ nanoparticles samples. The values of the lattice parameters and their variation with Mn doping concentration agree with earlier observation [27]. All the XRD peaks matched with the magnetite $Fe_3O_4$ phase, thus confirming that all the three synthesized nanoparticles are single-phase magnetite $Fe_3O_4$. The precise scrutiny of the major (311) peak positions relative to each other clearly showed shifting of the peak due to doping as shown in Fig. 1b. The Vegard's law states that dopant alone cannot produce its own XRD peak but can shift the host peak [28]. Thus, the shift in major peak position confirmed Mn doping of $Fe_3O_4$ nanoparticles.

The Scherrer's equation and the Hall–Williamson's (H–W) relation were employed for the determination of the crystallite sizes L using the XRD data. The details of the determination of the crystallite size $L$ using Scherrer's equation and H–W relation for the as-synthesized nanoparticles are given in another paper of the authors [22, 29]. The obtained L values from the Scherrer's equation and H–W relation are tabulated in Table 2. The determined L values from the Scherrer's equation and H–W relation are in agreement with each other for each sample. The L data show that the crystallite size increases with doping concentration. This is because of the increase of the lattice parameter with the increase of doping concentration.

### SEM analysis

Fig. 2a–c shows the SEM images of the as-synthesized pure $Fe_3O_4$ and Mn-doped $Fe_3O_4$ nanoparticles. Fig 2a shows the SEM image of pure $Fe_3O_4$ nanoparticles. Fig. 2b is the SEM image of as-synthesized 10% Mn-doped $Fe_3O_4$ nanoparticles, whereas Fig. 2c is the SEM image of 15% Mn-doped $Fe_3O_4$ nanoparticles.

The SEM images of pure $Fe_3O_4$ nanoparticles and 10 and 15% Mn-doped $Fe_3O_4$ nanoparticles, clearly show that the nanoparticles are formed from the assortments of

Table 1 Obtained and standard EDAX data

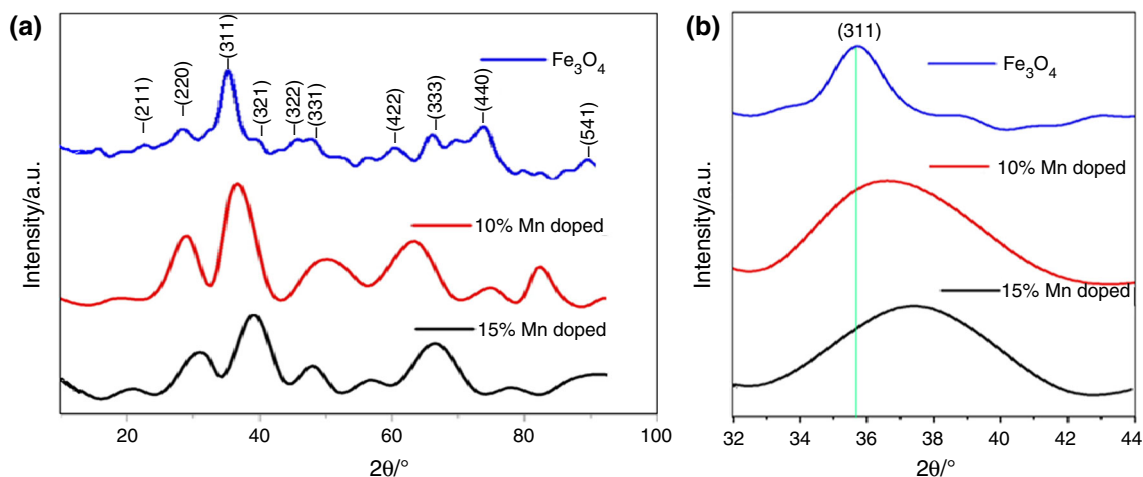| Element | $Fe_3O_4$ pure | | 10% Mn-doped $Fe_3O_4$ | | 15% Mn-doped $Fe_3O_4$ | |
|---------|------------------|------------------|------------------|------------------|------------------|------------------|
| | Observed mass/% | Calculated mass/% | Observed mass/% | Calculated mass/% | Observed mass/% | Calculated mass/% |
| Fe | 74.50 | 72.35 | 58.76 | 59.51 | 53.39 | 56.64 |
| O | 25.50 | 27.65 | 31.24 | 33.15 | 30.61 | 32.41 |
| Mn | – | – | 10.00 | 7.34 | 15.00 | 11.05 |
| Total | 100.00 | 100.00 | 100.00 | 100.00 | 100.00 | 100.00 |

**Fig. 1 a** X-ray diffraction patterns of as-synthesized nanoparticles, **b** (311) peaks shift

**Table 2** XRD parameters

| Sample | Lattice parameter/Å | Crystallite size L/nm | |
| --- | --- | --- | --- |
| | | Scherrer's equation | Hall–Williamson plot |
| Pure $Fe_3O_4$ | 8.392 | 7.20 | 6.58 |
| 10% Mn-doped $Fe_3O_4$ | 8.365 | 7.15 | 6.89 |
| 15% Mn-doped $Fe_3O_4$ | 8.368 | 7.89 | 7.25 |
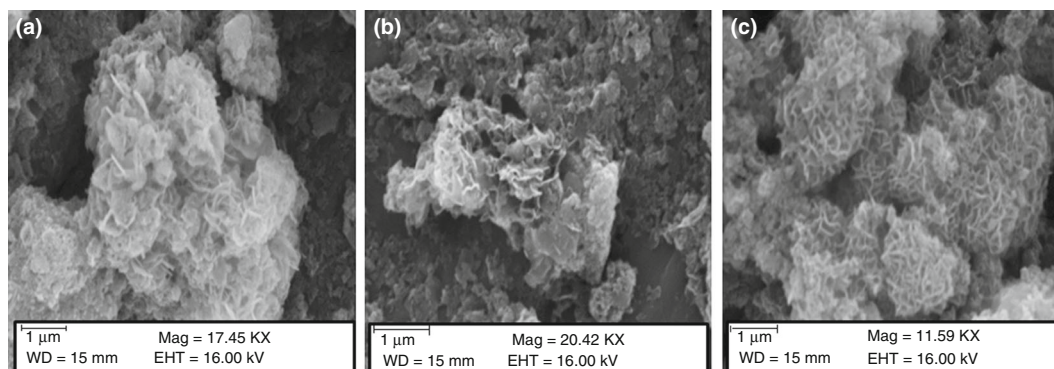


**Fig. 2** SEM images of the as-synthesized **a** pure, **b** 10%, and **c** 15% Mn-doped $Fe_3O_4$ nanoparticles

several nanosheets having voids among themselves. Similar SEM features have been reported earlier for Mn-doped $Fe_3O_4$ nanoparticles [30].

The thermal analysis of the as-synthesized nanoparticles samples is discussed in details in the next section. After the thermal analysis, the residual samples were collected and were characterized by SEM. Fig. 3a–c shows the SEM images of the pure $Fe_3O_4$ nanoparticles and 10 and 15% Mn-doped $Fe_3O_4$ nanoparticles after they have been thermally analyzed. The images show that the compact assorted nanosheet structure, Fig. 2, becomes completely dismantled into bits of individual sheets.

## Thermal analysis

The TG curves of pure and Mn-doped $Fe_3O_4$ nanoparticles are shown in Fig. 4.

The TG curves analysis shows that the pure $Fe_3O_4$ nanoparticles decompose in three steps, whereas the 10 and 15% Mn-doped $Fe_3O_4$ nanoparticles decompose in two steps. These three steps and two steps decompositions are substantiated by the respective DTG curves, Fig. 5.

The DTG curves show that the pure $Fe_3O_4$ nanoparticles have three peaks, whereas the 10 and 15% Mn-doped $Fe_3O_4$ nanoparticles show two peaks. The decomposition
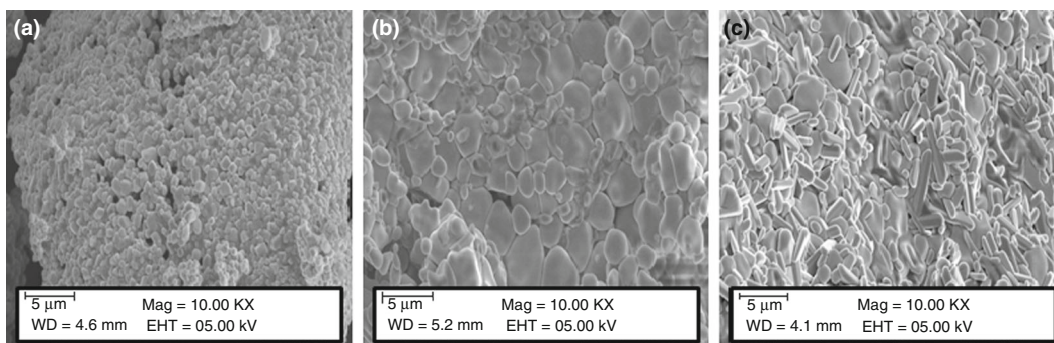
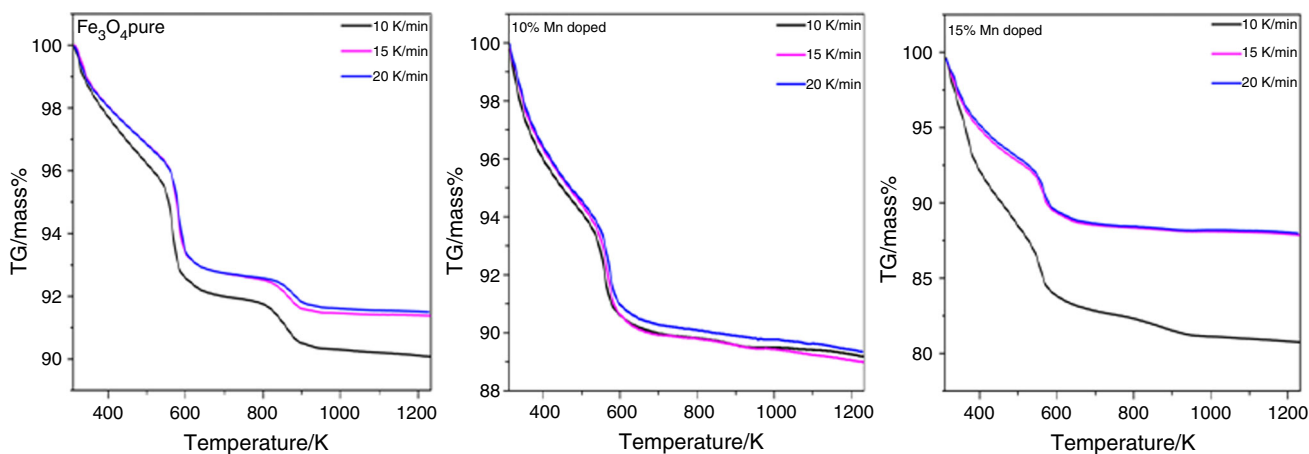**Fig. 3** SEM images of residual samples after thermal analysis of **a** pure, **b** 10%, and **c** 15% Mn-doped Fe$_3$O$_4$ nanoparticles



**Fig. 4** TG curves of pure Fe$_3$O$_4$ nanoparticles and 10 and 15% Mn-doped Fe$_3$O$_4$ nanoparticles
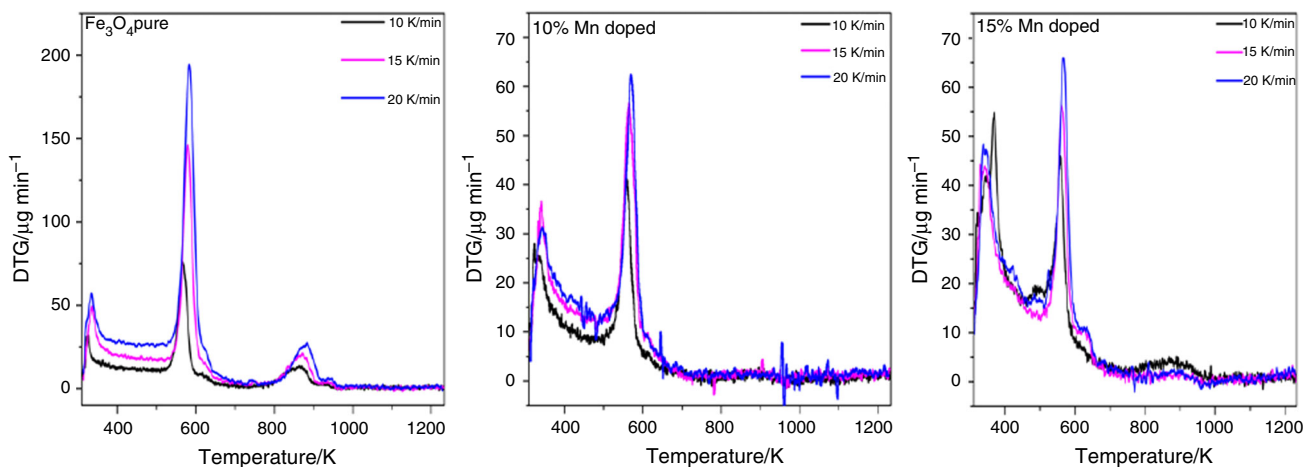


**Fig. 5** DTG curves of pure Fe$_3$O$_4$ and 10 and 15% Mn-doped Fe$_3$O$_4$ nanoparticles

starting temperature, total weight loss, DTG peak position and shift, etc. observed from the thermocurves for different heating rates are tabulated in Table 3.

The study of the data of Table 3 shows that as the heating rate increases, the TG weight loss percentage decreases for all the three samples. Also, the DTG peak positions shift toward high-temperature values with increase in heating rate. Both these observed phenomena corresponding to TG and DTG analyses are due to heat transfer limitation with faster rate of heating.

**Table 3** Total TG mass loss in percentage, DTG peaks position and shift observed

| Sample | Heating rate/ K min⁻¹ | Decomposition starting temperature/K | Total mass loss/% | DTG peak/K | | | | | |
|---|---|---|---|---|---|---|---|---|---|
| | | | | 1st peak | Shift | 2nd peak | Shift | 3rd peak | Shift |
| Fe₃O₄ | 10 | 311.33 | 9.85 | 321.91 | 0 | 565.69 | 0 | 862.64 | 0 |
| | 15 | 311.94 | 8.62 | 334.31 | 12.4 | 576.11 | 10.42 | 871.36 | 8.72 |
| | 20 | 311.99 | 8.46 | 335.13 | 13.22 | 583.13 | 17.44 | 881.79 | 19.15 |
| 10% Mn-doped Fe₃O₄ | 10 | 312.13 | 10.79 | 323.61 | 0 | 553.99 | 0 | – | – |
| | 15 | 312.98 | 10.57 | 337.22 | 13.61 | 559.30 | 5.31 | – | – |
| | 20 | 313.83 | 9.96 | 343.60 | 19.99 | 566.54 | 12.55 | – | – |
| 15% Mn-doped Fe₃O₄ | 10 | 314.57 | 18.86 | 324.68 | 0 | 556.54 | 0 | – | – |
| | 15 | 314.99 | 11.89 | 340.84 | 16.16 | 565.69 | 9.15 | – | – |
| | 20 | 315.53 | 11.58 | 345.31 | 20.63 | 570.15 | 13.61 | – | – |

The simultaneously recorded DTA curves for the three samples are shown in Fig. 6. The DTA curves show that in the initial temperature range, the behavior is exothermic (above zero level) followed by an endothermic nature (below zero level) till nearly 800 K, after that the DTA nature is again exothermic (above zero level). The initial exothermic nature may be due to the trapped water molecules converting to water vapor owing to increase in temperature and leaving the sample. The water vapor leaving the sample is corroborated by the weight loss observed in the same temperature region of the TG curves. Also, the restructuring of the nanoparticles might be taking place at the initial temperature. The restructuring of nanoparticles releases heat, which is observed here as an exothermic feature. It is also observed that the first exothermic peak shifts toward higher temperature values with increase in the heating rate. This behavior is observed in case of all the three samples. This is due to the heat transfer limitation with increase in heating rate. The endothermic curves have a peak around 580 K, and this is due to the reported thermal decomposition at 603 K [31]. This transition is owing to initiation of magnetite ($Fe_3O_4$) to maghemite ($\gamma$-$Fe_2O_3$) decomposition [14].

The exothermic nature of DTA curves after nearly 800 K in case of all the three samples and for all the three heating rates was due to the decomposition of the nanoparticles. The decomposition of the nanoparticles samples is substantiated by the SEM analysis of the thermal analyzed residual samples, Fig. 3. Minor peaks are observed in the temperature range of 930–950 K for different heating rates. These peaks are prominent in case of pure $Fe_3O_4$, but are minor kinks in case of doped samples. The kinks smoothen with increase in doping concentration from 10 to 15%. These exothermic peaks correspond to the
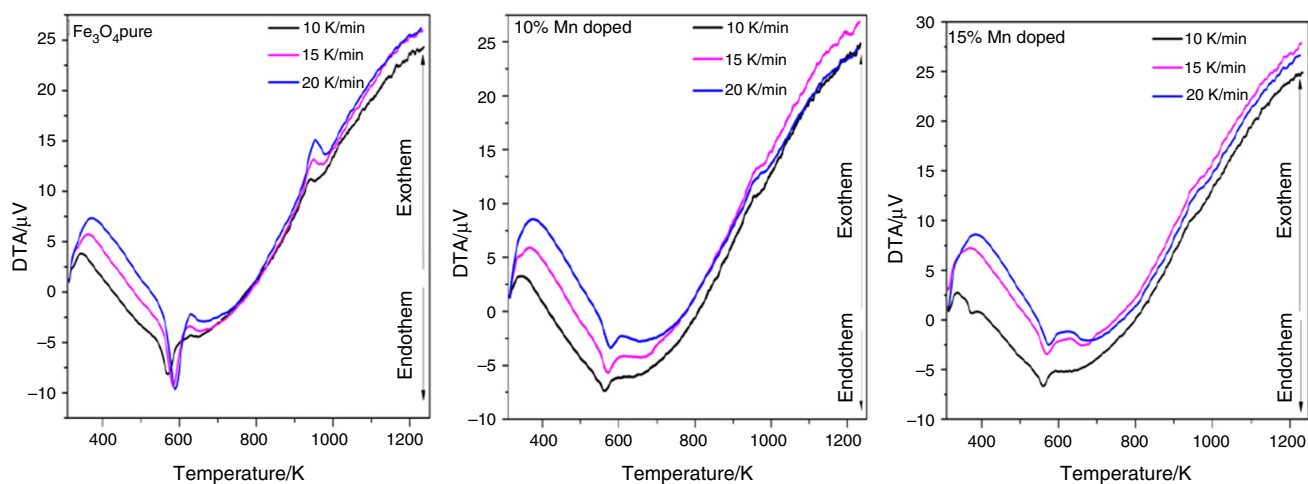


**Fig. 6** DTA curves of pure $Fe_3O_4$ and 10 and 15% Mn-doped $Fe_3O_4$ nanoparticles for three different heating rates of 10, 15, and 20 K min⁻¹

maghemite (γ-Fe$_2$O$_3$) to hematite (α-Fe$_2$O$_3$) phase transition, Fig. 7 [32]. The higher value of transition temperature (930–950 K) in present pure Fe$_3$O$_4$ nanoparticles sample compared to reported transition temperature may be due to dissimilar synthesis process. It is also observed that with increase in Mn$^{2+}$ doping concentration, the γ- to α-phase transition temperature increases as confirmed by smoothening of kinks. This indicates that Mn$^{2+}$ doping augments the phase stability of the magnetite nanoparticles in conformity with earlier report [33]. The mechanism involved is that, during phase transformation from maghemite to hematite, the lattice rearranges by relative sliding of the atomic layers and breaking of several Fe–O bonds. The effect of metal substitution on the thermal stability of maghemite can be explained as; with incorporation of substituting metals builds new bonds with oxygen (Mn–O) in the spinel structure and alters the strength of Fe–O bond. This is confirmed from the variation of lattice parameters obtained from XRD analysis, Table 2. The lattice parameter decreases with Mn doping compared to pure Fe$_3$O$_4$, thus the bond strength of Mn–O is more than the Fe–O leading to thermal stability of Mn doped magnetite. The decomposition leads to generation of heat shown over here as exothermic nature. The effect of heating rates on the DTA curves after nearly 800 K is negligible. This can be understood that due to high temperature of nearly more than 800 K, the decomposition of nanoparticles has started thus heating rates have no effect.

## Kinetic studies

The isoconversional method was employed for determination of the kinetic parameters of the as-synthesized pure and Mn-doped Fe$_3$O$_4$ nanoparticles from the recorded thermocurves. The isoconversional method can be solved in linear and nonlinear mode. The techniques of the linear mode are Friedman (FR) [34], Flynn–Wall–Ozawa (FWO) [35, 36], Kissinger–Akahira–Sunose (KAS) [37], and Li–Tang (LT) [38]. In these linear mode techniques, the activation energy is calculated from the slope of a straight line. In nonlinear modes, there are the integral [39, 40] and differential [41] methods, where the activation energy is calculated from a specific minimum condition. The nonlinear differential method and the modified nonlinear integral method use integration of the rate equation over small ranges of variables, lead to results similar to those obtained by the Friedman linear differential method. The nonlinear integral method [39] shows the results close to those derived applying the FWO and KAS methods [42]. Thus in this paper, the linear isoconversional KAS method was used.

Dehydration of solid hydrates is a solid-state phenomenon and is given as [43, 44]:

A(solid) → B(solid) + C(gas)
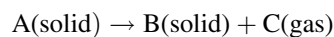
The kinetics of such reactions can be understood by taking into consideration the in-between equations. The reaction rate depends on the degree of conversion α (the ratio between the weight loss at moment t and the total weight loss at the end of dehydration) and its temperature dependence factor. Thus,

$$\frac{d\alpha}{dt} = k(T)f(a) \qquad (1)$$

where $t$ is the time, $T$ is the temperature, $k(T)$ is the Arrhenius rate constant, and α is the degree of conversion given by,
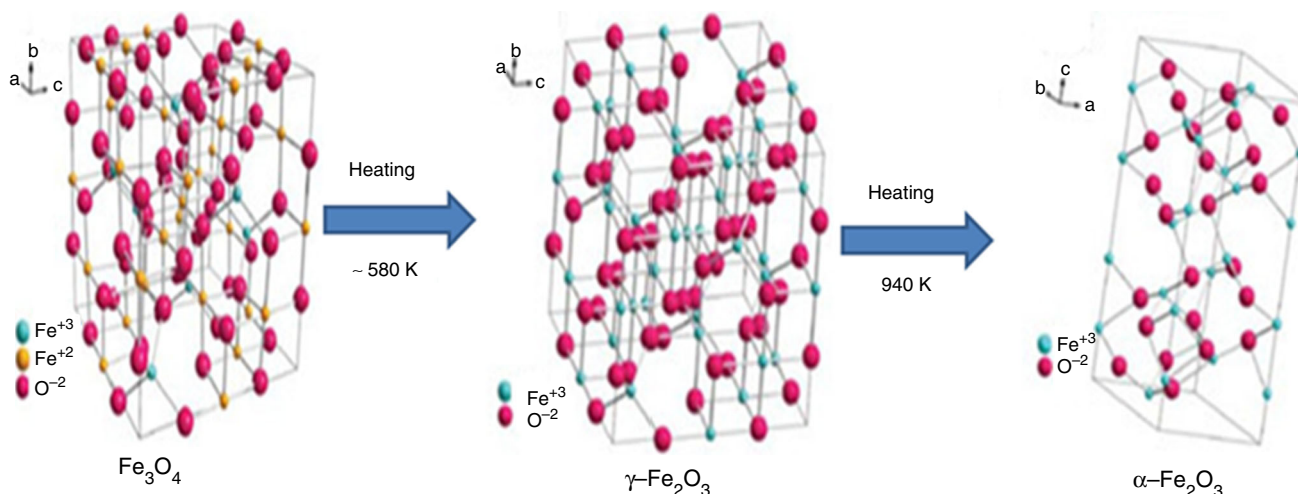


Fig. 7 Schematic illustration showing the decomposition and temperature range of the thermal transformation of Fe$_3$O$_4$ to γ-Fe$_2$O$_3$ to α-Fe$_2$O$_3$

$$\alpha = \frac{W_i - W_t}{W_i - W_f} \tag{2}$$

where $W_i$, $W_t$, and $W_f$ are the initial, actual, and final mass of the sample, respectively, and $f(\alpha)$ is the reaction model associated with a certain reaction mechanism. The direct temperature dependence of the rate constant is obtained by replacing $k(T)$ with the Arrhenius equation in Eq. (1),

$$k = A \exp\left(-\frac{E_a}{RT}\right) \tag{3}$$

where $A$ (the pre-exponential factor) and $E_a$ (the activation energy) are the Arrhenius parameters, and $R$ is the gas constant (8.314 J mol$^{-1}$ K$^{-1}$).

The KAS [34] method is an isoconversional linear integral method given in Eq. (4) form as:

$$\ln\frac{\beta}{T_P^2} = \ln\frac{AR}{g(\alpha)E_a} - \frac{E_a}{RT_P} \tag{4}$$

where $\beta$ is the heating rates, and $T_p$ is DTG peak temperature; $g(\alpha) = (W_\alpha - W)/W$, where $W_\alpha$ is the total mass loss in the reaction, and $W$ is the mass loss at absolute temperature $T$; and $E_a$ is the activation energy. For $\alpha = $ constant, the plot of $\ln(\beta/T_P^2)$ versus $1/T_P$, obtained from thermocurves recorded for three different heating rates gives a straight line whose slope allows calculation of the activation energy. The KAS plots for all the three as-synthesized pure and Mn-doped Fe$_3$O$_4$ nanoparticles are shown in Fig. 8. The activation energy $E_a$ for the three samples was calculated from the slopes of the plots and is tabulated in Table 4.

The frequency factor $A$, enthalpy change $\Delta H^*$, the entropy change $\Delta S^*$, and the free energy change (Gibbs function) $\Delta G^*$ were calculated using the following Eqs. (5–8) [45],

$$k = A \exp\left(-\frac{E}{RT}\right) \tag{5}$$

$$\Delta H^* = E - RT \tag{6}$$

$$\Delta S^* = 2.303 \log\left[\frac{Ah}{k_B T}\right] R \tag{7}$$

$$\Delta G^* = \Delta H^* - T\Delta S^* \tag{8}$$

Here, $T$ is the DTG peak temperature, $k$ is rate constant, $k_B$ is Boltzmann constant, and $h$ is Planck's constant. The obtained values of $E_a$, $A$, $\Delta H^*$, $\Delta S^*$, and $\Delta G^*$ for the as-synthesized pure Fe$_3$O$_4$, 10% Mn, and 15% Mn-doped Fe$_3$O$_4$ nanoparticles are tabulated in Table 4. The three steps in pure Fe$_3$O$_4$ as well as two steps in 10 and 15% Mn-doped Fe$_3$O$_4$ nanoparticles shown in Table 4 were decided from the TG steps as well as from the number of DTG peaks. The data show that the $E_a$ has the maximum values in the last steps of each sample. That means in pure Fe$_3$O$_4$, it is step 3, whereas in case of 10 and 15% Mn-doped Fe$_3$O$_4$, it is step 2. The maximum values of $E_a$ in the last steps are due to the phase transition leading to decomposition of the compounds in these temperature ranges. The obtained results of maximum value of the activation energy in the last region for the three samples are supported by the values obtained from the enthalpy change and entropy change. The enthalpy change values are highest in the last step. That means maximum heat is absorbed in this last step of respective samples leading to decomposition of the sample. The decomposition of the sample increases the entropy which is also highest in this last step. Hematite is more stable phase than maghemite as the former has a more compact crystal structure (hexagonal) than the later (cubic). So during the phase transition from maghemite to hematite, the excess energy is released from the system which gives rise to an exothermic peak. The amount of energy released or absorbed ($\Delta H^*$) during a phase
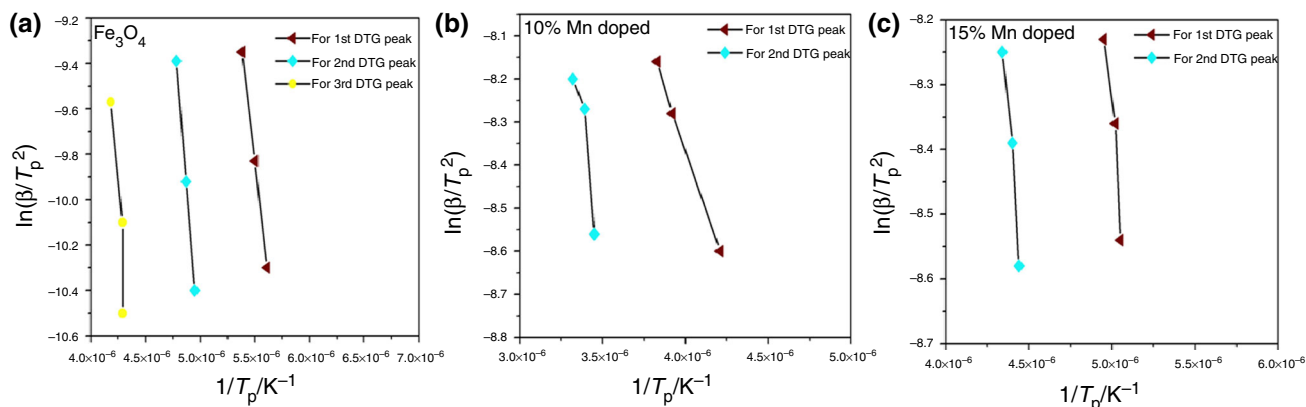


Fig. 8 Kissinger–Akahira–Sunose (KAS) plots for **a** pure Fe$_3$O$_4$, **b** 10% Mn-doped Fe$_3$O$_4$, and **c** 15% Mn-doped Fe$_3$O$_4$ nanoparticles

**Table 4** Kinetic parameters evaluated by the nonmechanistic equations for as-synthesized pure and 10 and 15% Mn-doped $Fe_3O_4$ nanoparticles

|  | Steps | Avg. DTG Peak $T_p$/K | $E_a$/kJmol$^{-1}$ | $A$/m$^{-1}$ | $\Delta H^*$/kJmol$^{-1}$ | $\Delta S^*$/kJmol$^{-1}$ | $\Delta G^*$/kJmol$^{-1}$ | $R$ |
|---|---|---|---|---|---|---|---|---|
| $Fe_3O_4$ | 1 | 332.29 | 43.01 | $1.69 \times 10^7$ | 40.25 | $-12.89$ | 44.40 | 0.913 |
|  | 2 | 576.70 | 153.75 | $6.09 \times 10^{14}$ | 148.96 | 2.66 | 164.70 | 0.987 |
|  | 3 | 874.92 | 243.51 | $2.63 \times 10^{14}$ | 236.23 | 3.92 | 233.90 | 0.955 |
| 10% Mn-doped $Fe_3O_4$ | 1 | 340.11 | 18.76 | $1.49 \times 10^4$ | 15.89 | $-136.54$ | 23.94 | 0.992 |
|  | 2 | 564.57 | 86.60 | $1.77 \times 10^8$ | 81.90 | $-63.78$ | 117.91 | 0.943 |
| 15% Mn-doped $Fe_3O_4$ | 1 | 345.85 | 27.54 | $5.64 \times 10^2$ | 19.98 | $-23.27$ | 71.15 | 0.946 |
|  | 2 | 562.16 | 99.04 | $5.56 \times 10^4$ | 94.36 | $-19.17$ | 105.14 | 0.927 |

transition determines the feasibility of a transition. For $\Delta H^* > 0$, the energy is absorbed by the system.

## Conclusions

The pure $Fe_3O_4$ and 10 and 15% Mn-doped $Fe_3O_4$ nanoparticles were synthesized by simple wet chemical reduction technique. The EDAX of all the three as-synthesized nanoparticles showed that they are stoichiometric and do not contain any impurity. The XRD analysis of all the three as-synthesized nanoparticles showed them to possess cubic structure. The determined lattice parameters were in agreement with the standard and reported data. The crystallite sizes determined from the XRD data using Scherrer's equation and Hall–Williamson's relation were in agreement with each other. The SEM analysis of the pure, 10 and 15% Mn-doped $Fe_3O_4$ nanoparticles showed that the nanoparticles are formed from the assortment of several nanosheets. The structures formed from the nanosheets have voids among themselves. The SEM analysis of the residual samples of the nanoparticles after thermal analysis showed that the assorted nanosheets get dismantled into bits.

The simultaneously recorded TG and DTG curves of the pure $Fe_3O_4$ and 10 and 15% Mn-doped $Fe_3O_4$ nanoparticles in the temperature range of 308–1233 K for three different heating rates of 10, 15, and 20 K min$^{-1}$ in nitrogen atmosphere showed that the thermal decomposition takes place by three steps for pure $Fe_3O_4$ and two steps for both 10 and 15% Mn-doped $Fe_3O_4$ nanoparticles. The simultaneously recorded DTA curves of all the three as-synthesized samples showed initial exothermic nature followed by an endothermic nature up to nearly 800 K and above that it showed exothermic nature. The initial exothermic nature arises due to vaporization of entrapped water molecules and restructuring of nanoparticles. The subsequent endothermic curves state heat absorption by the nanoparticles. The heat absorption is substantiated by weight loss observed in the corresponding TG curves in the same temperature range. The endothermic curves have a peak around 580 K, arising due to transition from magnetite ($Fe_3O_4$) to maghemite ($\gamma$-$Fe_2O_3$). The DTA exothermic nature above nearly 800 K states decomposition of the nanoparticles leading to release of heat. Minor DTA peaks are observed in the temperature range of 930 K to 950 K for different heating rates. These peaks are prominent in case of pure $Fe_3O_4$, but appear as minor kinks in case of doped samples. The kinks smoothen with increase in doping concentration from 10 to 15%. These DTA exothermic peaks correspond to the maghemite ($\gamma$-$Fe_2O_3$) to hematite ($\alpha$-$Fe_2O_3$) phase transition. Smoothening of the peaks in case of 15% Mn-doped $Fe_3O_4$ nanoparticles compared to 10% Mn-doped $Fe_3O_4$ nanoparticles for all three heating rates affirms enhancement of the maghemite ($\gamma$-$Fe_2O_3$) to hematite ($\alpha$-$Fe_2O_3$) transition temperature with increase in Mn doping. The kinetic parameters determined employing KAS method showed that the values of the activation energy $E_a$, enthalpy change, and entropy change are maximum in the last decomposition steps of each sample. The positive large enthalpy change values in the last steps state heat absorption by the samples. Heat absorption by the samples leads to its decomposition, also being manifested in the TG curves by weight loss. The samples' decomposition leads to disorder being substantiated by larger values of entropy. The larger weight loss observed in the last steps of each sample leads to larger values of activation energy $E_a$ as observed for that steps.

# References

1. Kinemuchi Y, Ishizaka K, Suematsu H, Jiang W, Yatsui K. Magnetic properties of nanosize $NiFe_2O_4$ particles synthesized by pulsed wire discharge. Thin Solid Films. 2002;407:109–13.
2. Sugimoto M. The past, present, and future of ferrites. J Am Ceram Soc. 1999;82:269–80.
3. Pati S, Philip J. Effect of cation trapping on thermal stability of $Fe_3O_4$ nanoparticles. J Nanosci Nanotechnol. 2014;14:4114–23.
4. Machala L, Tucek J, Zboril R. Polymorphous transformations of nanometric iron(III) oxide: a review. Chem Mater. 2011;23:3255–72.
5. Xiaobin X, Mingyuan G, Cen W, Jiang J. High temperature stable mono disperse superparamagnetic core-shell iron-oxide@$SnO_2$ nanoparticles. Appl Phys Lett. 2009;95:183112–3.
6. Tsedev N, Shinpei Y, Mikio T. Thermal properties of the $\gamma$-$Fe_2O_3$/poly(methyl methacrylate) core/shell nanoparticles. Solid State Sci. 2005;7:33–6.
7. Ayyappan S, Panneerselvam G, Antony M, Rao N, Thirumurugan N, Bharathi A, Philip J. Effect of initial particle size on phase transformation temperature of surfactant capped $Fe_3O_4$ nanoparticles. J Appl Phys. 2011;109:084303–8.
8. Gnanaprakash G, Ayyappan S, Jayakumar T, Philip J, Raj B. Magnetic nanoparticles with enhanced $\gamma$-$Fe_2O_3$ to $\alpha$-$Fe_2O_3$ phase transition temperature. Nanotechnology. 2006;17:5851–7.
9. Xisheng Y, Dongsheng L, Zhengkuan J, Lide Z. The thermal stability of nanocrystalline maghemite $Fe_2O_3$. J Phys D Appl Phys. 1998;31:2739–44.
10. Chang-Woo L, Sung-Soo J, Jai-Sung L. Phase transformation of $\beta$-$Fe_2O_3$ hollow nanoparticles. Mater Lett. 2008;62:561–3.
11. Jian C, Jinghai Y, Lili Y, Maobin W, Bo F, Donglai H, Lin F, Bingji W, Hao F. The effects of doping and shell thickness on the optical and magnetic properties of Mn/Cu/Fe-doped and Co-doped ZnS nanowires/ZnO quantum dots/$SiO_2$ heterostructures. J Appl Phys. 2012;112:014316–8.
12. Sidhu S, Gilkes J, Posner M. The behavior of Co, Ni, Zn, Cu, Mn, and Cr in magnetite during alteration to maghemite and hematite Soil Sci. Soc Am J. 1980;44:135–8.
13. Sidhu P. Transformation of trace element-substituted maghemite to hematite. Clays Clay Miner. 1988;36:31–8.
14. Sarda C, Rousset A. Thermal stability of barium-doped iron oxides with spine structure. Thermchim Acta. 1993;222:21.
15. Pati S, Singh J, Ochoa M, Guimaraesa M, Sales A, Coaquira H, Oliveira A, Garg K. Facile approach suppress $\gamma$-Fe2O3 to $\alpha$-Fe2O3 phase transition beyond 600 °C in Fe3O4 nanoparticles. Mater Res Express. 2015;2:045003–12.
16. Lai J, Shafi M, Loos K, Ulman A, Lee Y, Vogt T, Estournes C. Doping $\gamma$ Fe2O3 nanoparticles with Mn(III) suppresses the transition to the $\alpha$-Fe2O3 structure. J Am Chem Soc. 2003;125:11470–1.
17. Vichery C, Maurin I, Bonville P, Boilot P, Gacoin T. Influence of protected annealing on the magnetic properties of $\gamma$-Fe2O3 nanoparticles. J Phys Chem C. 2012;116:16311.
18. Wang J, Chen Q, Zeng C, Hou B. Magnetic-field-induced growth of single-crystalline $Fe_3O_4$ nanowires. Adv Mater. 2004;16:137–40.
19. Jianjun L, Hongming Y, Guodong L, Yanju L, Jinsong L. Cation distribution dependence of magnetic properties of sol–gel prepared $MnFe_2O_4$ spinel ferrite nanoparticles. J Magn Magn Mater. 2010;322:3396–400.
20. Amighian J, Mozaffari M, Nasr B. Preparation of nano-sized manganese ferrite ($MnFe_2O_4$) via co-precipitation method. Phys Stat Sol. C. 2006;3:3188–92.
21. Chao L, Bingsuo Z, Adam R, Zhang ZJ. Reverse micelle synthesis and characterization of superparamagnetic $MnFe_2O_4$ spinel ferrite nanocrystallites. J Phys Chem B. 2000;104:1141–6.
22. Chaki S, Malek T, Chaudhary M, Tailor J, Deshpande M. Magnetite $Fe_3O_4$ nanoparticles synthesis by wet chemical reduction and their characterization. Adv Nat Sci Nanosci Nanotechnol. 2015;6:035009.
23. Malek T, Chaki S, Tailor J, Deshpande M. Thermal decomposition study of Mn-doped $Fe_3O_4$ nanoparticles. In: AIP conference proceedings; 2016. vol. 1728, p. 020390-5.
24. Budrugeac P, Segal E. Applicability of the Kissinger equation in thermal analysis. J Therm Anal Calorim. 2007;88:703–7.
25. Kissinger H. Reaction kinetics in differential thermal analysis. Anal Chem. 1957;29:1702–6.
26. Zhao M, Song Z. Synthesizing kinetics and characteristics for spinel $LiMn_2O_4$ with the precursor using as lithium-ion battery cathode material. J. Power Source. 2007;164:822–8.
27. Warner LC, Chouyyok W, Mackie EK, Neiner D, Saraf VL, Droubay CT, Warner GM, Addleman SR. Manganese doping of magnetic iron oxide nanoparticles: tailoring surface reactivity for a regenerable heavy metal sorbent. Langmur. 2012;28:3931–7.
28. Chaki S, Chaudhary M, Deshpande M. Effect of indium and antimony doping in SnS single crystals. Mater Res Bull. 2015;63:173–80.
29. Malek T, Chaki S, Chaudhary M, Tailor J, Deshpande M. Study of the effect of Mn doping on Fe3O4 nanoparticles synthesized by wet chemical technique. 2017; (submitted manuscript).
30. Gherca D, Pui A, Cornei N, Cojocariu A, Nica V, Caltun O. Synthesis, characterization and magnetic properties of $MFe_2O_4$ (M = Co, Mg, Mn, Ni) nanoparticles using ricin oil as capping agent. J Magn Magn Mater. 2012;324:3906–11.
31. Lu Z, Yang L, Guo Y. Thermal behavior and decomposition kinetics of six electrolyte salts by thermal analysis. J Power Source. 2006;156:555–9.
32. Gillot B, Nouaim H, Mathieu F, Rousset A. Effect of a pre-treatment under high-pressure on the oxidation mechanism of magnetite to $\gamma$-Fe2O3 and on the transformation $\gamma$-Fe2O3 to $\alpha$-Fe2O3. Mater Chem Phys. 1991;28(4):389–97.
33. Pati S, Philip J. Afacile approach to enhance the high temperature stability of magnetite nanoparticles with improved magnetic property. J Appl Phys. 2013;113:044314–9.
34. Friedman H. Kinetics of thermal degradation of char-foaming plastics from thermogravimetry. Application to a phenolic plastic. J Polym Sci. C. 1963;6:183–95.
35. Flynn J, Wall L. General treatment of the thermogravimetry of polymers. J Res Natl Bur Stand A Phys Chem A. 1966;70:87–523.
36. Ozawa T. A new method of analyzing thermogravimetric data. Bull Chem Soc Jpn. 1965;38:1881–6.
37. Akahira T, Sunose T. Joint convention of four electrical institutes. Research report (Chiba Institute of Technology). Chiba. 1971;16:22–31.
38. Li C, Tang T. Dynamic thermal analysis of solid-state reactions. J Therm Anal. 1997;49:1243–8.
39. Vyazovkin S, Dollimore D. Linear and nonlinear procedures in isoconversional computations of the activation energy of non isothermal reactions in solid. J Chem Inf Comput Sci. 1996;36:42–5.
40. Vyazovkin S. Modification of the integral isoconversional method to account for variation in the activation energy. J Comput Chem. 2001;22:178–83.
41. Budrugeac P. Differential non-linear isoconversional procedure for evaluating the activation energy of non-isothermal reactions. J Therm Anal Calorim. 2002;68:131–9.

42. Budrugeac P, Segal E. Some methodological problems concerning nonisothermal kinetic analysis of heterogeneous solid–gas reactions. Int J Chem Kinet. 2001;33:564–73.

43. Vlaev L, Nikolova M, Gospodinov G. Non-isothermal kinetics of dehydration of some selenite hexahydrates. J Solid State Chem. 2004;177:2663–9.

44. Vyazovkin S. A unified approach to kinetic processing of nonisothermal data. Int J Chem Kinet. 1996;28:95–101.

45. Yakuphanoglua F, Gorgulub A, Cukurovali A. An organic semiconductor and conduction mechanism: N-[5-methyl-1,3,4-tiyodiazole-2-yl] ditiyocarbamate compound. Phys B. 2004;353:223–9.